Journal of the Brazilian Society of Mechanical Sciences and Engineering (2023) 45:320
https://doi.org/10.1007/s40430-023-04096-y

TECHNICAL PAPER

Determining hyper-viscoelastic structural properties of UHMWPE material used in Prodisc-C prosthesis employing a finite element–optimization coupling method

Sana Ghafarmoghadam[1] · Alireza Seifzadeh[1,2] · Ali Mokhtarian[2] · Reza Abedinzadeh[2]

Received: 12 August 2022 / Accepted: 7 February 2023 / Published online: 22 May 2023
This is a U.S. Government work and not under copyright protection in the US; foreign copyright protection may apply 2023

Abstract
Choosing an appropriate material that owns favorable mechanical properties for decreasing wear and increasing the lifespan of the prosthesis is of great importance. This study aimed to determine the Prodisc-C prosthesis structural properties using the finite element coupling method and optimization algorithm. Another goal was to discuss and evaluate the von Mises stress and mechanical properties of Prodisc-C prosthesis including hyper-viscoelastic and viscoelastic properties. For this purpose, a two-dimensional model was built and further was simulated and discussed using Abaqus software. The model's mechanical properties were obtained via an annealing optimization algorithm. The algorithm aimed to create conformity between stress relaxation diagrams achieved from each step of simulation and experimental tests. The obtained results confirmed a high similarity in terms of conformity between the optimized behaviors achieved from finite element based on the Moony–Rivlin and Neo-Hooke models and stress relaxation test results. Afterward, the acquired characteristic parameters were then employed in a three-dimensional structural model of Prodisc-C prosthesis to evaluate von Mises stress distribution under a compressive load of 73.6 N. After considering the hyper-viscoelastic properties of Moony–Rivlin for the upper part of the prosthesis, which was composed of cobalt, the maximum stress in the prosthesis was determined to be 429.7 MPa. However, for the lower part, which was composed of titanium, the stress was calculated to be 35 MPa. Moreover, the stress of the prosthesis polymeric core was evaluated to be 936 MPa, indicating an improvement in comparison to Neo-Hooke and prosthesis elastic properties.

Keywords UHMWPE material · Optimization · Finite element · Hyper-viscoelastic · Prodisc-C prosthesis

1 Introduction

The human spine is one of the most crucial musculoskeletal structures of the body. It owns a complex structure that is responsible for protecting the spinal cord as well as bearing a large percentage of the body's weight. Overall, the structure of the spine is similar to a fibrous cushion, which operates as a shock absorption system for the spine [1].

Figure 1 illustrates a section of the cervical spine, which consists of seven cervical vertebrae that are placed on top of each other. Furthermore, the intervertebral disc, which is cartilage-like to a cushion piece, is allocated between the two vertebrae. It is vital to note that parts of this disc are eradicated, and the disc becomes flattered with its flexibility diminished due to aging, which further results in the disc being easily damaged [2]. The cervical disc prostheses are designed to act as a replacement for normal disc functions as the disc deteriorates, which allows the spine to function

Technical Editor: João Marciano Laredo dos Reis.

✉ Alireza Seifzadeh
seifzadeh@iaukhsh.ac.ir

Sana Ghafarmoghadam
Sana.ghafarimoghadam@iaukhsh.ac.ir

Ali Mokhtarian
mokhtarian@iaukhsh.ac.ir

Reza Abedinzadeh
abedinzadeh@iaukhsh.ac.ir

[1] Department of Biomedical Engineering, Khomeinishahr Branch, Islamic Azad University, Khomeinishahr, Isfahan, Iran

[2] Department of Mechanical Engineering, Khomeinishahr Branch, Islamic Azad University, Khomeinishahr, Isfahan, Iran

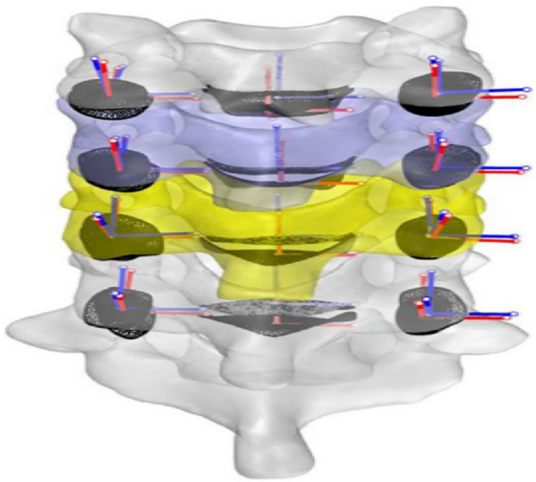

Fig.1 Cervical spine [3]

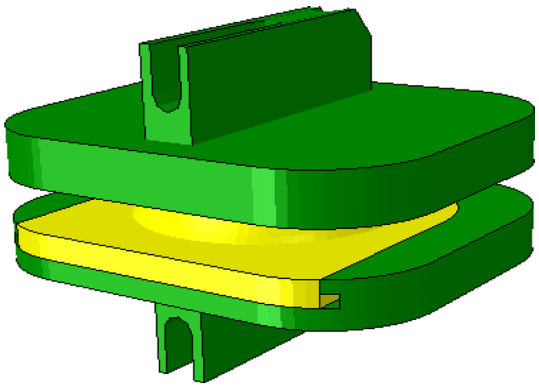

Fig. 2 Geometric modeling of Prodisc-C based on prosthesis model pattern of Moussa et al. [4]

naturally so that the replaced disc performs similarly to a normal disc in all situations.

The employment of cervical disc prosthesis is considered one of the greatest and novel achievements in the biomedical engineering field. It can be said that most cervical disc prostheses possess a spherical and bowl structure. They mainly consist of three crucial parts: an upper plate, a lower plate, and a polymeric material, which is allocated between the two plates. The wear of the implants' contact surfaces is one of the major drawbacks of the cervical disc prosthesis, which leads to the reduction of the prosthesis' lifespan. It is noteworthy to mention that Prodisc-C is one of the most prominent artificial cervical disc models.

Figure 2 depicts a geometrical design of Prodisc-C in the form of a ball and a socket (which is the most common dynamic prosthesis in the treatment industry). According to Fig. 2, the aforementioned disc is composed of two metallic upper and lower plates which are made of chromium–cobalt (CoCrMo) and titanium (Ti6AI4 V), respectively. Besides, the central core, placed between the two metallic plates, is made of UHMWPE polymer.

It is known that ultra-high molecular weight polyethylene (UHMWPE) is one of the most widely used polymers, which is of great importance in medical fields. This polymer is used as the central core of the cervical and lumbar discs because of the significant wear between their slip surfaces. It can be argued that wear resistance is one of the remarkable properties of UHMWPE material; this fact has made UHMWPE material a worthy candidate for a wide range of engineering applications. Note that the material becomes more durable as the molecular weight of polyethylene increases. UHMWPE is classified as a type of engineering plastic that possesses a set of favorable advantages, including high wear resistance, impact resistance, low friction coefficient, corrosion resistance, and resistance against chemical change [5].

Furthermore, the nonlinear elastic analysis has gained substantial attention due to the growth of developed materials and structures as well as the need for analyzing their behavior. The nonlinear nature of the governing equations and the lack of access to the material's behavioral equations are considered two major drawbacks in solving nonlinear elasticity problems. It can be stated that the first problem has been addressed to a certain extent due to the everyday improvement and development of numerous numerical methods, especially the finite element (FE) method. However, the same is not true for the second drawback as it stays unsolved [6, 7]. There are various categories of materials with immense capability in elastic deformations, such as elastomers and polymers. To better describe their behavior, it is possible to make use of the structural relationships of hyper-viscoelastic materials, which can be expressed based on the strain standard utilized in the energy-strain function [8]. Viscoelastic and hyperelastic equations are two most commonly used types of equations to express the polymer's behavior. The hyperelastic materials show a nonlinear behavior against the applied force. Despite a large displacement, they maintain their elastic behavior. Contrary to the viscoelastic equations, the effect of time is not applied in hyperelastic equations. The use of viscoelastic equations for expressing rubber behavior is rather appropriate, as it takes the creep effect of the rubber structure into account. Viscoelastic equations are obtained by combining the Prony series and hyperelastic equations. Finally, by combining the two, the structural relations of viscoelastic and incompressible hyperelastic are obtained by considering the effect of strain rate [9–11].The hyperelasticity of the materials makes the material's behavior completely nonlinear [12]. UHMWPE materials possess viscoelastic properties [8]. Therefore, these materials are considered hyper-viscoelastic due to their significant deformations, nonlinear stress–strain relationship, and time-dependent properties. Since it is not possible to analytically obtain the viscoelastic properties of the

rubber-like materials predicting the transient region of its response, it is necessary to use a trial and error method such as finite element [13]. Coupling the finite element model with the optimization algorithm makes it possible to obtain the optimal rubber-like structural properties with high accuracy [14]. The trial and error method, FE coupling method, and optimization algorithm (FE/OPT) were employed by Seifzadeh et al. [14] to obtain the properties of the articular cartilage samples. They used the data obtained from the stress relaxation test and a reversed FE method to determine the properties of sheep's cartilage material with engineered texture. In another study, they obtained the pro-hyper-viscoelastic properties of cartilage by using the FE model and combining them with the optimization method [14]. Nazouri et al. utilized a material property coupling method (FE/OPT) to mechanically characterize polyvinyl alcohol hydrogel [13]. Moreover, Mahdian et al. took advantage of the material properties of coupling method to acquire the mechanical properties of human corneal tissue [15]. In Niki et al., the compression stress relaxation test was conducted on rat tibia bone specimens for normal ($n=5$) and osteoporotic ($n=5$) groups to characterize their mechanical properties using the coupling (FE/OPT) algorithm. Through this method, the structural equation parameters of the Neo-Hooke model and the Prony series coefficients were used to describe the hyperelastic and the viscoelastic behaviors of specimens, respectively [15, 16]. In previous investigations, UHMWPE materials used in Prodisc-C prosthesis have been considered as a linear elastic material that has several limitations in high strains. For example, the polymer's elastic properties were considered by Moussa et al. [4], and thereafter, the von Mises stress was obtained by using SolidWorks software. Moreover, John et al. (2013) acquired the stress value by simulating and analyzing the Prodisc-C prosthesis in Abaqus software without considering the hyper-viscoelastic properties of the UHMWPE central [17].

Hyperelastic and viscoelastic properties of UHMWPE have been overlooked in prior studies [15]. Under physiological stresses, UHMWPE experiences more than 5% strain deformation and exhibits finite nonlinear distortion. As a result, its behavior may be anticipated using models that take into account finite deformation. In this respect, no prior work has been published on the use of a FE model and its conjunction with a method to optimize the nonlinear hyper-viscoelastic properties (namely bulk modulus and shear modulus) of UHMWPE material in agreement with the experimental findings of stress relaxation. This study scrutinized this subject. To predict the mechanical behavior of rubber-like materials and to study the damage and degradation of these materials, it is necessary to obtain their stress–strain distribution. Calculating the optimized structural properties of rubber-like materials is necessary for obtaining their stress–strain distribution for these materials which show nonlinear behavior. Also, strain energy functions are required to obtain their structural properties in order to predict their response. Therefore, one of the objectives of this study was to determine the structural properties of the UHMWPE material used in the cervical disc prosthesis. UHMWPE hyper-viscoelastic properties were estimated using Moony–Rivlin and Neo-Hooke hypotheses. Besides, the stress distribution of von Mises was determined using Moony–Rivlin and Neo-Hooke models and was compared with the behavior of the elastic model for analysis and assessment of Prodisc-C prosthesis.

2 Materials and methods

The present study was performed in two experimental and numerical parts. UHMWPE material properties were determined in the laboratory using the stress relaxation test. In the numerical part, the properties of UHMWPE materials were obtained using the FE/OPT coupling method. Furthermore, to simulate the behavior of cervical disc prosthesis, it was analyzed and investigated in Abaqus software.

2.1 Unconfined stress relaxation test

In the laboratory of Isfahan University of Technology (device name: SANTAM), three sections of UHMWPE cylindrical samples with a radius of 10 mm and an elevation of 15 mm [18] having grade 1000 were exposed to compression testing. It was, therefore, possible to measure the stress relaxation responsiveness of the specimens under varied loading conditions (Fig. 3). For maximal force endurance, the stress relaxation response of a specimen was chosen as the best candidate.

Ten steps of force application were utilized during the compression test on the sample, with a loading velocity of

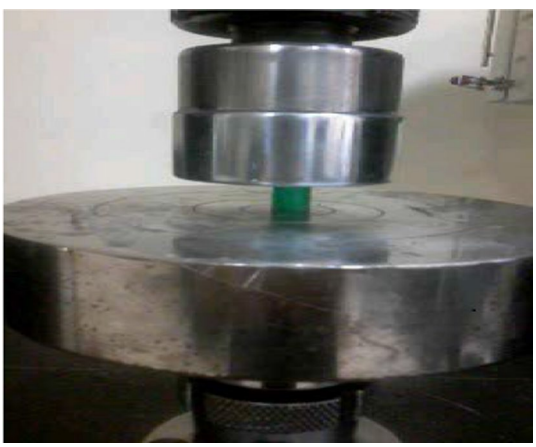

Fig. 3 Stress relaxation testing on a cylindrical UHMWPE sample

1.5 mm/min [18]. The sample was loaded in such a manner that each loading resulted in a 0.6 mm displacement. The force was then reapplied after 60 s. The method of exerting compressive force up to a 30% strain was therefore successfully completed.

2.2 Simulation of finite element

Using the FE in Abaqus software, the infinite stress relaxation test on UHMWPE was simulated based on the configuration of Fig. 3 and the test described in Sect. 1.2 is in line with the compression test specifications [14]. The sample dimensions of 10 mm in radius and 15 mm in height [18] were taken into account in the simulation. An isotropic hyper-viscoelastic material, UHMWPE, was proposed. Additionally, the Moony–Rivlin and Neo-Hooke models were employed to characterize the material's constructive activity. The coefficient of friction between the top plate and the specimen was determined to be 0.42 in earlier investigations [19]. As illustrated in Fig. 4, the bottom plate was also fixed. According to the test procedure, one of the loading situations in this simulation, which was imposed through ten ramps, was applied to the top plate, and meshing was conducted following the study of Seifzadeh et al. [14].

2.3 Optimization of structural parameters

To determine the parameters of the sample materials, the FE/OPT coupling method developed by Seifzadeh et al. [20] was utilized. The optimization was accomplished by coding in MATLAB software based on the SA optimization algorithm. When used in conjunction with other statistical optimization algorithms, the SA optimization algorithm has the potential to locate the general optimum point during the search environment of optimization parameters. Using a coded optimization algorithm, the isotropic hyper-viscoelastic structural equations' parameters of the Moony–Rivlin and Neo-Hooke models, determined based on the estimation of the strain energy function per unit volume (Appendix A), were created in MATLAB and then sent to the Abaqus software as input data. This input was employed to compute the temporal responsiveness of the force transmitted to the specimen in Abaqus, and the difference between the estimated response and the response observed in the experimental measurement was utilized to determine the error value. It was subsequently forwarded to the MATLAB optimization method as a target function by relying on the response force's sum of squares difference (SSD) (Eq. (1)) [21, 22].

$$\mathrm{SSD} = \sum_{i=1}^{n} \left\{ \left[F^{\mathrm{FEM}}(x\mathrm{opt}.t)\right]_i - \left[F^{\mathrm{EXP}}(t)\right]_i \right\}^2 \tag{1}$$

where F_i^{FEM} and F_i^{EXP} are the data for the force output coming from modeling and experimental compression assessments, respectively. xopt denotes the vector of the optimized material parameters, and N represents the number of sites at which the forces generated from the FE modeling are compared with the empirical forces. Owing to the detected error, MATLAB transmitted new values as material parameters to the Abaqus document input. This algorithm was repeated until the error between the FE response and the experimental measurement was reduced to an acceptable level [14–19, 21–23]. The Simulated Annealing (SA) optimization algorithm was used to investigate throughout the parameters domain during 100 trials and errors. By searching the entire domain, this algorithm increases and decreases the material parameters to converge to the optimized final result. For all the optimized parameters, the lowest and highest values were entered in the SA optimization toolbox located in MATLAB software. These lowest and highest values were obtained by trial and error and by monitoring the trend of the graph obtained from FE compared with the experimental results. For the normalized shear and bulk moduli used in the Prony series, the values in the range of 0–1 defined by the Abaqus manual were considered for this purpose [20–22].

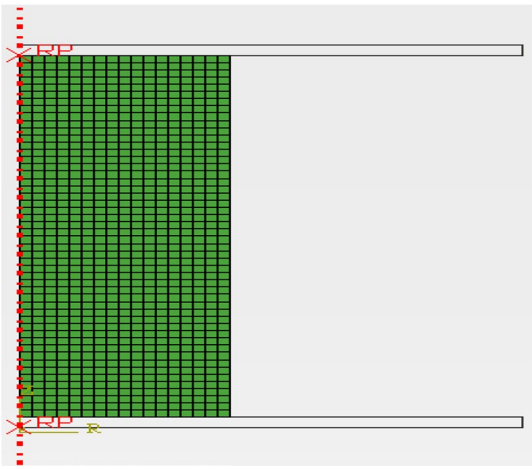

Fig. 4 Geometry and meshing of the FE model used for simulation in the Abaqus software

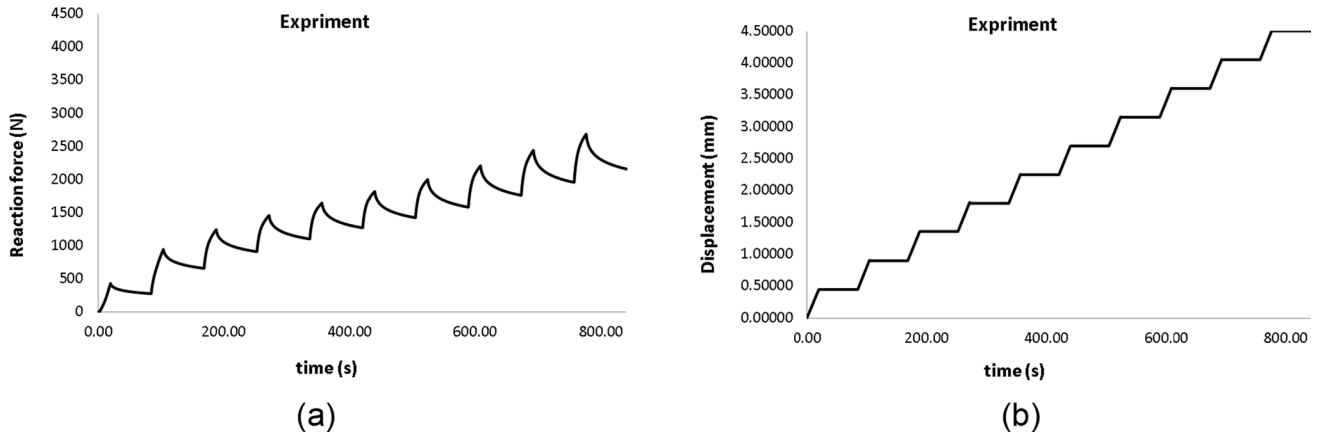

Fig. 5 **a** Force–time diagram obtained for the specimen during stress relaxation pressure test and **b** displacement–time diagram applied to the specimen during stress relaxation pressure test

Table 1 Optimized structural parameters for UHMWPE using the Moony–Rivlin and Neo-Hooke models

Material parameters	Neo-Hooke	Moony–Rivlin
C_{10} (MPa)	8,219,178	5,900,000
C_{01} (MPa)	–	2,319,179
D(MPa)	$1*10^{-8}$	$1*10^{-8}$
g_1	0.49	0.49
g_2	0.286	0.286
g_3	0.15	0.15
k_1	0.49	0.385
k_2	0.286	0.271
k_3	0.15	0.27
τ_1	10	10
τ_2	490	340
τ_3	200	300
K_0(MPa)	200	200
μ_0(MPa)	16.44	16.44
E (MPa)	48	48
ν	0.46	0.46

3 Results and discussion

Figure 5a exhibits the results of a compression analysis on a UHMWPE specimen using a compressive force of up to 30% strain, and Fig. 5b displays the stress relaxation response (force–time diagram) of the specimen.

3.1 Outcomes of optimization

Through a FE coupling optimization method, it is possible to accurately anticipate the behavior of UHMWPE by incorporating isotropic hyper-viscoelastic properties. In this regard, there were 12 fundamental parameters in total: three parameters (C_{10}, C_{01}, D) explain hyperelastic behavior, while the remaining nine parameters (g_1, g_2, g_3, k_1, k_2, k_3, τ_1, τ_2,τ_3) describe viscoelastic actions (Table 1). Up to 230 iterations were carried out during the optimization process. Figure 6a, b compare the force recorded by the stress relaxation test for the two models of Moony–Rivlin (large strain) and Neo-Hooke (small strain) with the force anticipated by structural equations. The parameters were determined via FE/OPT coupling method for UHMWPE. The Neo-Hooke model's projected force (Fig. 6a) was found to be less compatible with the force recorded during stress relaxation testing compared to the Moony–Rivlin model's anticipated force (Fig. 6b), particularly at higher strains. Table 1 presents the FE/OPT coupling method's ideal parameters for Neo-Hooke and Moony–Rivlin models.

There were two strain-forming component constants) $\bar{I}_1$,$\bar{I}_2$) in the strain energy function per starting volume used by the Moony–Rivlin model, according to Appendix A. However, the strain energy in the Neo-Hooke model's initial volume unit was composed of just one constant representing the strain-forming component ($\bar{I}_1$). In this way, we predicted that the material's behavior using the Moony–Rivlin model would be closer to experimental findings since the Moony–Rivlin model allowed for more structural properties to be searched for than the Neo-Hooke model. Nevertheless, the ideal performance of the material based on the two models of Moony–Rivlin and Neo-Hooke produced findings that were consistent with those obtained in the experiments. The optimization objective function used in the FE/OPT coupling method was the error calculated by Eq. 1. The error was calculated by comparing the force obtained using the finite element

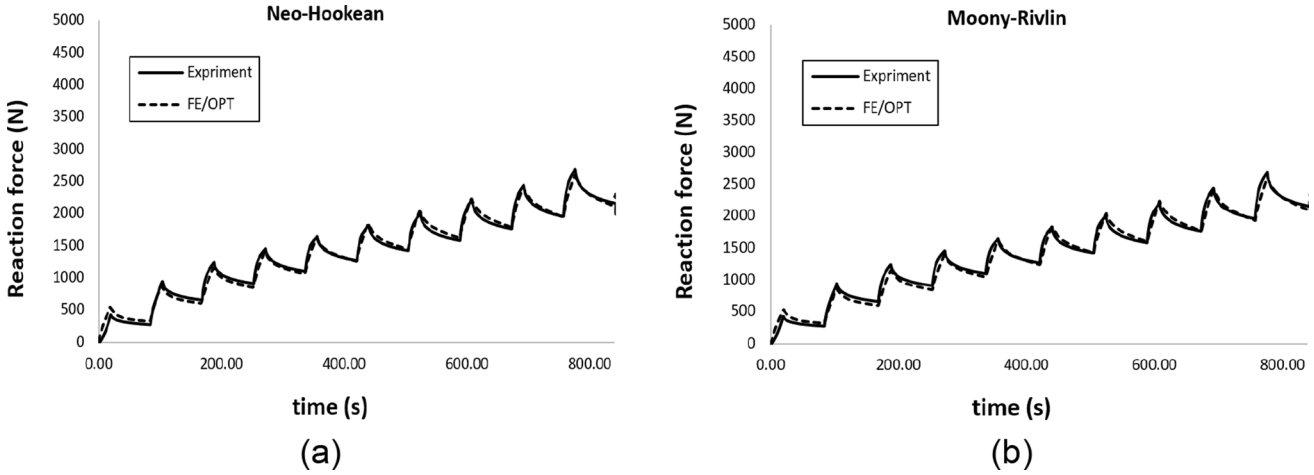

Fig. 6 **a** Comparison of the measured force and force predicted by the coupling method (FE/OPT) for UHMWPE using the Neo-Hooke model and **b** using the Moony–Rivlin model

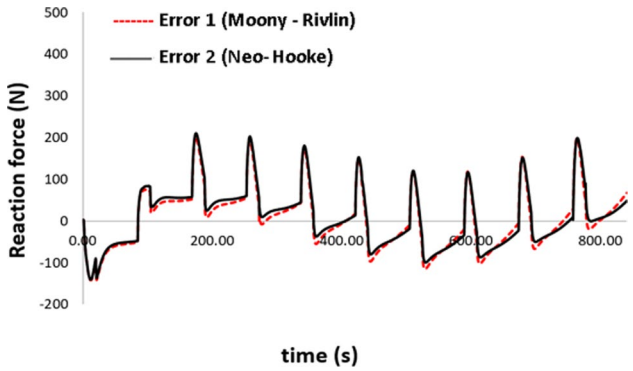

Fig. 7 Difference between experimental force and force predicted by the (FE/OPT) coupling method in the Moony–Rivlin and Neo-Hooke models

model with the one obtained from the experimental results. In each iteration, the error was acquired by the FE/OPT coupling method using Eq. 1 for both Moony–Rivlin and Neo-Hook models. It should be noted that in this case, the optimization error according to the Moony–Rivlin model was "error 1 = 2.2849e + 07," which was somewhat different from the optimization error relying on the Neo-Hooke model, which was "error 2 = 2.3613e + 07". As for the experimental stress relaxation force of the UHMWPE material, Fig. 7 shows the graphs of the force differential between the FE/OPT coupling based on the Moony–Rivlin and Neo-Hooke models.

Table 1 presents the ideal optimization process of structural parameters for the two models examined in this study. In addition, Eqs. 4 and 7 (Appendix A) were employed to determine the bulk modulus (K_0) and shear modulus (μ_0) of UHMWPE for the Moony–Rivlin and Neo-Hooke models, respectively. A strong correlation was found between the best-matching results from the two models, as can be observed in the graphs.

To investigate the effect of the behavior of the Moony–Rivlin model on each of the structural parameters, we performed the sensitivity analysis of the model for the hyperelastic and viscoelastic parameters separately.

3.2 Sensitivity analysis for hyperelastic parameters

Figure 8 displays the force–time graphs obtained from the simulation in comparison to the experimental results. It also exhibits the calculated response of the specimen using a 30% increase and decrease of the optimized hyperelastic parameters using the Moony–Rivlin model.

Because the shear modulus was directly connected to the C_{10} parameters in Eqs. (3) and (5) (Appendix A), there was a direct connection between the C_{10} parameter and the compressive force applied to the specimen model. The force produced from the FE rose as a result of increasing C_{10} by 30%. The intensity of force was also reduced when the C_{10} parameter was lowered by 30% (Fig. 8a).

Similar to C_{10} and force, there was a direct link between C_{01} and force. Figure 8b shows the same findings for parameter C_{01} in the Moony–Rivlin model.

There was an inverse relationship between parameter D and the force applied on the sample model (Fig. 8c). To explain this, consider Eq. 4 (Appendix A), in which the bulk modulus is directly related to the force and the bulk modulus is inversely related to parameter D. Thus, the loading force reduced as D grew, and it increased as D dropped.

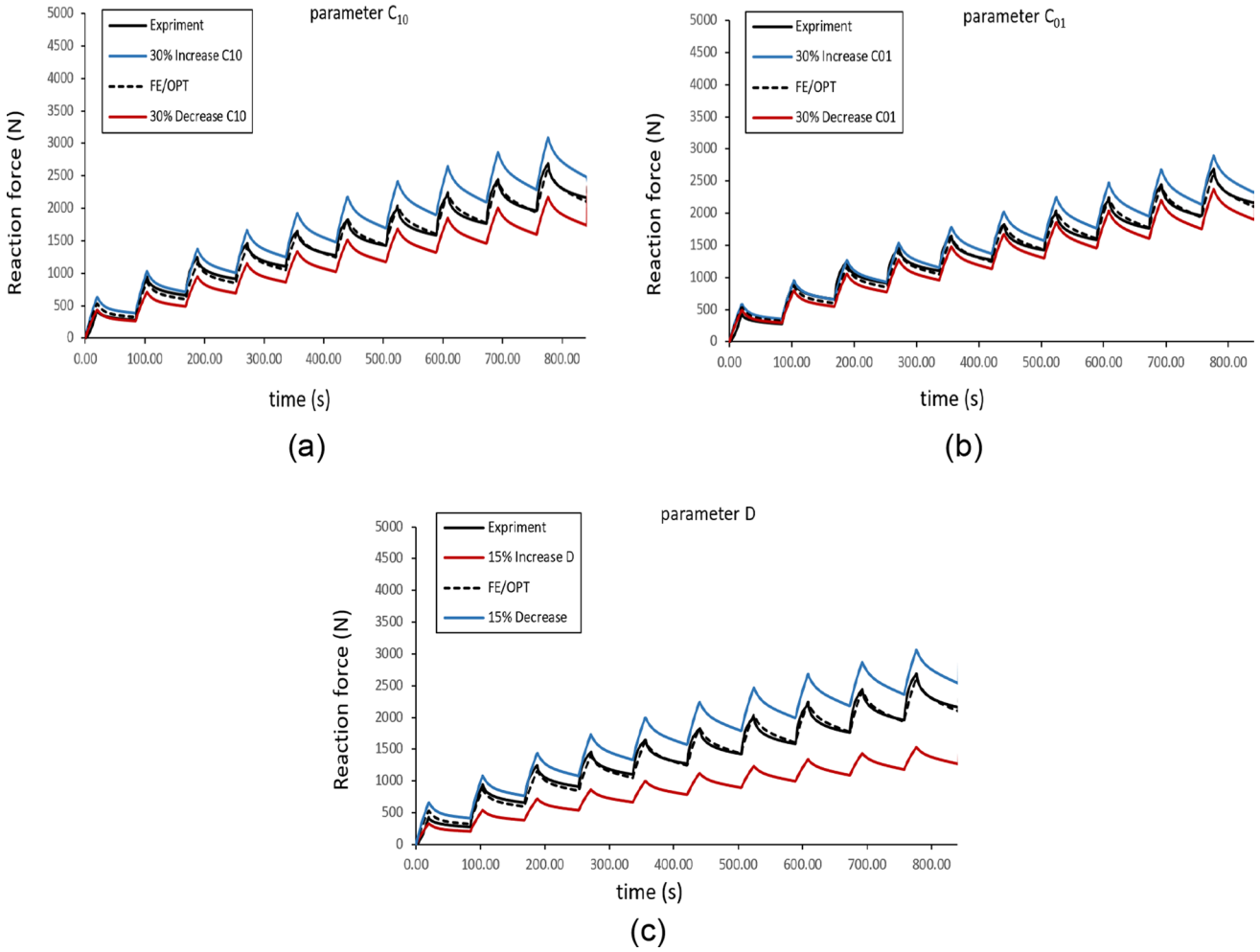

Fig. 8 Effect of increasing and decreasing hyper elastic parameters (C_{10}, C_{01}, D) on the force resulting from the FE

3.3 Sensitivity analysis for viscoelastic parameters

The results of increasing and decreasing values of the viscoelastic parameters in the Moony–Rivlin model can be observed in the force–time diagrams obtained using the coupled FE/OPT method in comparison with the experimental results (Fig. 9).

The maximum force on each ramp grew considerably with a 15 percent increase in the value of these parameters, and the force was balanced with a steeper slope because of the direct link between τ, g, k , and force. The minimum force per ramp was lowered by a 15% reduction of these values, and the force was balanced by slowing the slope (Figs. 9a, 9b, and 9c).

4 Analysis of the stress of cervical disc prosthesis

To employ UHMWPE as a core in the cervical disc prosthesis, it was necessary to determine its properties. In this respect, a three-dimensional simulation of a cervical disc prosthesis (Prodisc-C) was developed in SolidWorks software according to the optimal dimensions of the Prodisc-C prosthesis shape established by [4] for stress evaluation (Fig. 10). Prodisc-C total disc replacement is a prosthesis that has a cobalt chrome/polyethylene bearing surface and is semi-constrained. It was developed based on the design of the Prodisc-L lumbar disc arthroplasty. The material

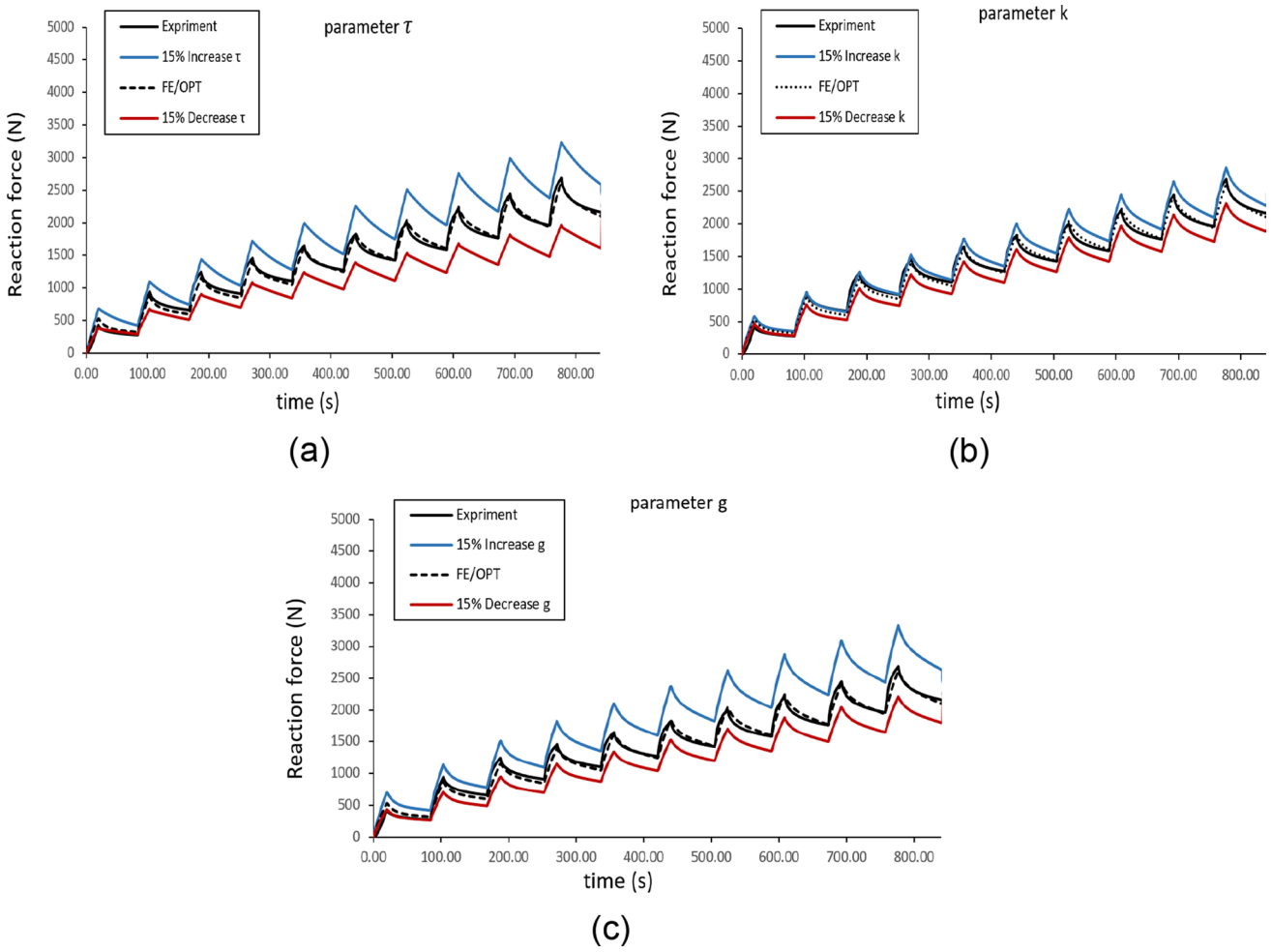

Fig. 9 Effect of increasing and decreasing hyperelastic parameters (g_i, k_i, τ_i) on the force resulting from the FE

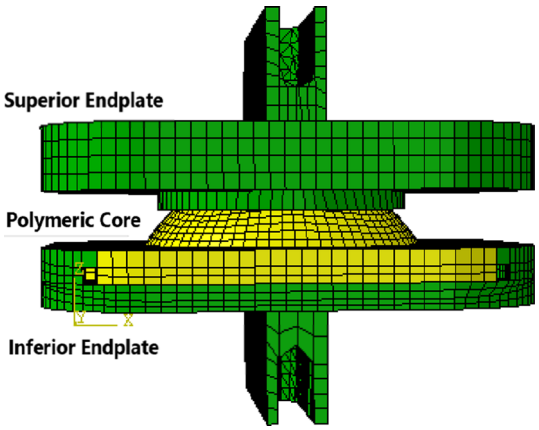

Fig. 10 FE meshing model of a prosthesis (Prodisc-C) composed of two metal end plates and a central component of the polymeric core

properties of the top plate containing chromium–cobalt alloy ($E = 220{,}000$ MPa, $v = 0.32$) and the bottom plate containing titanium ($E = 114{,}000$ MPa, $v = 0.35$) [17–24], as well as the material properties of the UHMWPE core using optimum hyper-viscoelastic parameters which were determined by FE/OPT coupling method, are reported in Table 1 (according to the Neo-Hooke and Moony–Rivlin models in two distinct phases). Static loading was also applied during this investigation. The polymer core was attached to the bottom plate (titanium) based on the biomechanical behavior of the backbone discs. In one study [19–25], a "hard contact" simulation with a friction coefficient of 0.2 was utilized to model sliding connections between the polymer core and the top plate (chromium–cobalt) [26]. The upper plate was loaded, while the underlying plate was fastened in all directions. Hexagonal elements (C3D8R) which were decreased by using eight-node elements were employed to mesh the upper and bottom plates of the polymer core. The number of elements in the polymer core, top, and bottom plates was 7096, 13,625, and 5619, respectively (Fig. 10). The model also underwent mesh sensitivity testing and response convergence. The top plate was subjected to a compressive force of 73.6

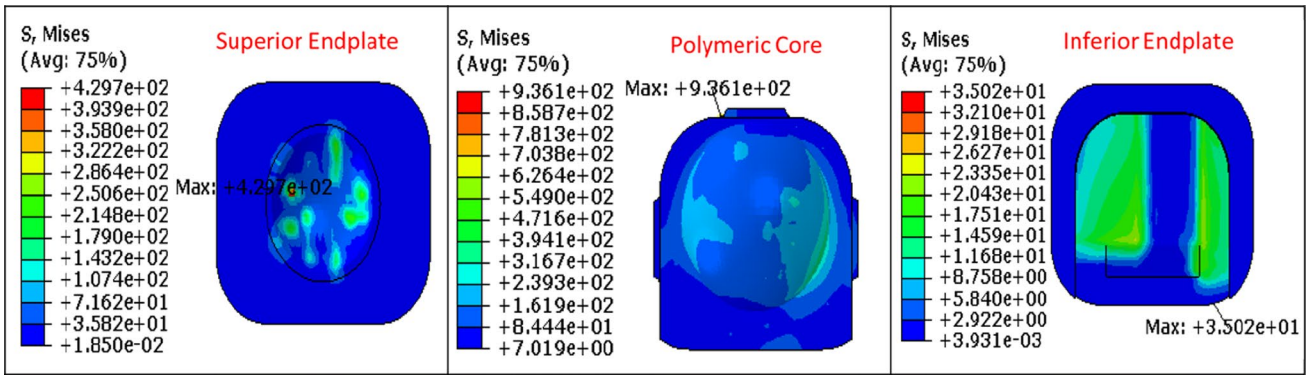

Fig. 11 Von Mises stress contour on three Prodisc-C prostheses (assuming the hyper-viscoelastic properties of polymer using the Moony–Rivlin model)

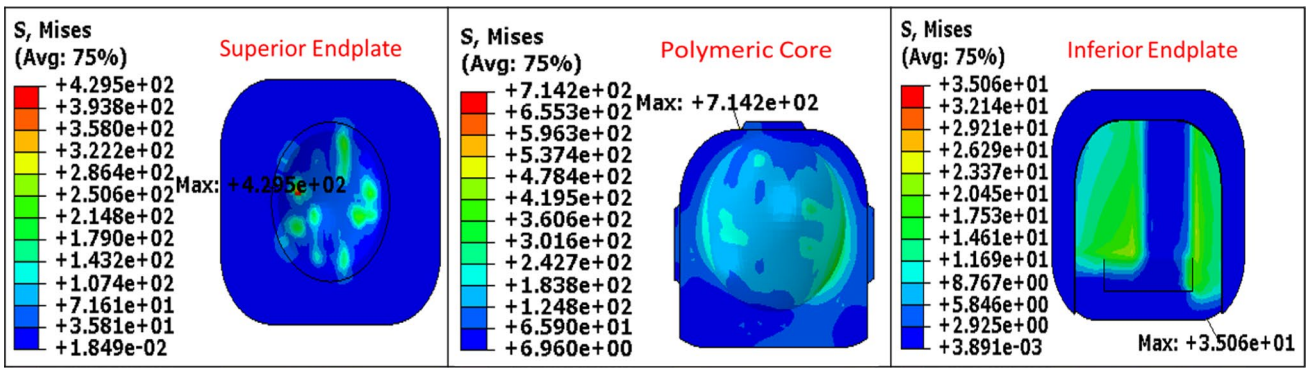

Fig. 12 Von Mises stress contours on three parts of Prodisc-C prosthesis (assuming the hyper-viscoelastic properties of polymer using Neo-Hooke model)

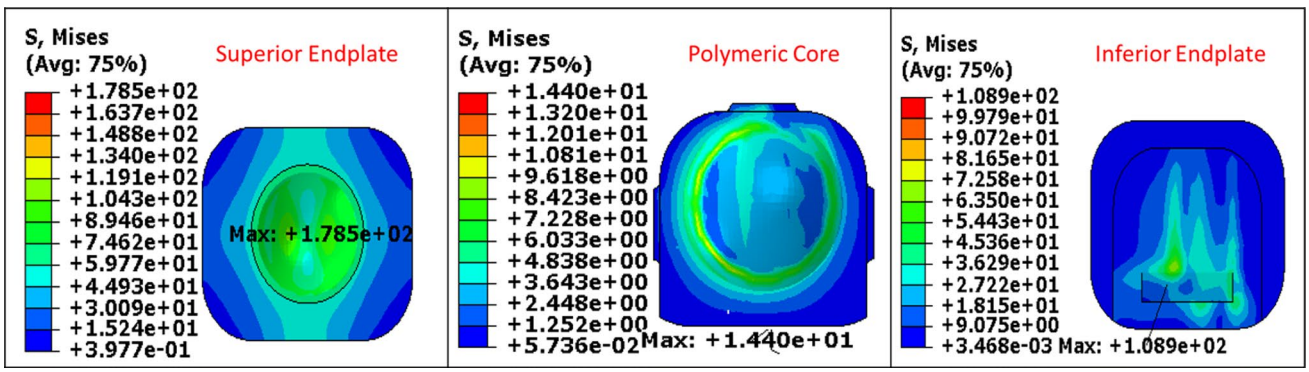

Fig. 13 Von Mises contour on three parts of Prodisc-C prosthesis by assuming the elastic properties of the polymer

N, which is equivalent to the spectrum of human head weight [27].

Figures 11–12 depict von Mises stress contours on the Prodisc-C prosthesis following modeling, assuming the ideal attributes of the Prodisc-C prosthesis polymer nucleus containing hyper-viscoelastic construction according to the Moony–Rivlin and Neo-Hooke models, correspondingly.

Additionally, a prosthesis stress evaluation was conducted under comparable border and loading circumstances, but solely the elastic properties of the core structure of the disc prosthesis were taken into account to analyze the effect of

the hyper-viscoelastic properties of the core of the Prodisc-C prosthesis.

Figure 13 illustrates the von Mises stress dispersion on the Prodisc-C prosthesis when only the elastic properties of the polymer were examined by employing the values obtained from the FE/OPT coupling method (Table 1).

There was a substantial difference between the stress distribution of the elastic properties and the hyper-viscoelastic properties of the polymer (Figs. 11–13).

To calculate the von Mises stress using the Mooney-Rivlin and Neo-Hooke models, the amount and rate of loading and the loading conditions have been the same for all; since the polymer has a viscoelastic behavior at any moment of loading, the bulk and shear moduli change. They also vary with the change in the loading rates. So, it is impossible to compare the results in this study with those in the previous ones quantitatively. However, for a qualitative verification, a comparison can be made with previous studies. John Mo et al. estimated the maximum von Mises stress for the upper plate to be 675 MPa using the elastic properties for the polymer [17]. In the current study, according to the hyper-viscoelastic properties obtained from the experimental results conducted on the polymer, the maximum von Mises stress was estimated to be 429 MPa. The maximum von Mises stress in the Moony–Rivlin model for chromium–cobalt, titanium, and polymer was 429.7, 35, and 936 MPa, respectively. Also, the maximum von Mises stress in the Neo-Hooke model for chromium–cobalt, titanium, and the polymer was 429.5, 35, and 714.2 MPa, respectively. However, using the elastic properties for the polymer, the maximum von Mises stress calculated for chromium–cobalt, titanium, and the polymer was 178.5, 108.9, and 14.4 MPa, respectively. Thus, in comparison, the von Mises stress calculated using the elastic properties for the UHMWPE is smaller than the one calculated using the hyper-viscoelastic properties for the UHMWPE polymer.

5 Conclusion

Through the FE/OPT coupling method, ten parameters of the hyper-viscoelastic constitutive equation of UHMWPE polymer were determined using stress relaxation experimental tests (Table 1). The von Mises stresses in a Prodisc-C prosthesis were also calculated using a three-dimensional model of it containing the optimized UHMWPE hyper-viscoelastic structural parameters. The UHMWPE hyper-viscoelastic properties were used to create a FE model considering all nonlinearities inherently existing in the polymer including tension–compression, strain stiffening, and finite deformation nonlinearities. The hyper-viscoelastic structural model used for UHMWPE simulation to predict the Prodisc-C prosthesis load-bearing characteristics also considers the viscoelastic property of the polymer. Since the polymer bulk and shear moduli are time dependent, the used model in this study takes into account these moduli time variations during loading. For the Neo-Hooke and Moony–Rivlin models, the UHMWPE hyper-viscoelastic properties were determined. It was evident from the force–time diagrams that when the Moony–Rivlin model was employed for FE response estimation as opposed to the Neo-Hooke model, the outcomes were quite comparable, which were consistent with the diagrams produced from the stress relaxation analyses. The sensitivity analysis were performed on the optimized hyper-viscoelastic structural parameters of UHMWPE. These parameters were changed by 30%, and the variation effects on the stress relaxation response were observed.

Then, a three-dimensional model of the Prodisc-C prosthesis was developed considering the UHMWPE intrinsic viscoelastic behavior. In the developed model, a hyper-viscoelastic strain energy function was also used for the UHMWPE including all its nonlinear properties, to predict the mechanical behavior of the implant in the body under designed loads and calculate von Mises stress in different parts of the prosthesis. A considerable difference in the stress contours of various parts of the cervical prosthesis was observed compared to the stress dispersion contours in the elastic model, which was detected as a result of the core's hyper-viscoelastic properties. The highest stress generated in the three parts of the Moony–Rivlin and Neo-Hooke models was much higher than that of the elastic model. To compare the von Mises stress in the Moony–Rivlin and Neo-Hook models, everything (such as the amount and rate of loading and the loading conditions as well as models' boundary conditions) was kept the same for all cases. Because the polymer has a viscoelastic behavior at any moment of a given loading and loading rate as well as in the various loading rates, the bulk and shear moduli all change. So, it is impossible to compare results in this study with those of previous ones quantitatively. But, for an estimation and a qualitative verification, a comparison can be made with previous studies. John Mo et al. estimated the maximum von Mises stress for the upper plate to be 675 MPa according to the elastic properties. In the current study, according to the hyper-viscoelastic properties obtained from the results of the experiments conducted on the polymer, the maximum von Mises stress was estimated to be 429 MPa.

Note that, rubber-like materials have nonlinear properties such as tension–compression, strain stiffening along with finite deformation resulting in a non-uniform stress–strain within it. They also have intrinsic viscoelasticity and also have shock absorption and energy dissipation properties, so for modeling such materials, it is inevitable to use the strain energy function like that of hyperelasticity for their characterization and to predict their load-bearing characteristics. The appropriate

Table 2 Abbreviations

Explanation	Lists of acronym
Optimization	OPT
Finite element	FE
Coupled finite element–optimization	FE/OPT
Sum of the squared difference	SSD
Annealing optimization algorithm	SA
Hyperelastic	HE
Strain energy density	U
Modulus of Young	E
Poisson's ratio	ν
Shear moduli	μ_0
Bulk moduli	K_0
Shear deformation	λ_i
Constant of the strain deformation	$\bar{I}_i$
Material constant	$C10$ (MPa)
Prony series constant	g_i
Prony series constant	K_i
Deformation gradient	J
Shear moduli of relaxation	G_0
Non-dimensional shear moduli	$g\infty$
Non-dimensional bulk moduli	$k\infty$

mechanical properties are the best predictors of polymer load-bearing capacity in this implant.

Considering the relevance of the prosthesis's resistance to distortion, fracture, and notably friction on the contact surfaces, hyper-viscoelastic properties must be considered to produce reality-based modeling. The results of this study can be used to predict the transient response of the Prodisc-C prosthesis under different loading and loading conditions such as dynamic, static, and cyclic as well as different loading rates in a relatively higher strain (Table 2).

Appendix A: Energy function of strain

Because of the material's hyperelasticity, its function is fully nonlinear, and the material is capable of experiencing a significant amount of reversed distortion. The distortion gradient is used to construct the strain energy function per unit volume [28]. Hyperelastic material behavioral models based on strain energy function assessment, such as the Neo-Hooke and Moony–Rivlin models, are commonly employed in the simulation. Equation [29] is a function of the distortion tensor constants) $\bar{I}_1$ و $\bar{I}_2$(in the Moony–Rivlin model and expresses the strain energy function per unit volume (U).

$$U = C_{10}\left(\bar{I}_1 - 3\right) + C_{01}\left(\bar{I}_2 - 3\right) + \frac{1}{D_1}((J^{el} - 1))^2, \tag{2}$$

where C_{10}, C_{01}, and D_1 represent temperature-dependent variables, and $\bar{I}_1$ and $\bar{I}_2$ represent the initial and secondary constants of the strain-forming part, which are expressed in terms of shear distortion stretch as follows:

$$\bar{I}_1 = \bar{\lambda}_1^2 + \bar{\lambda}_2^2 + \bar{\lambda}_3^2, \quad \bar{I}_2 = \bar{\lambda}_1^{(-2)} + \bar{\lambda}_2^{(-2)} + \bar{\lambda}_3^{(-2)}, \tag{3}$$

where $(i = 1,2,3)$, $\bar{\lambda}_i = \lambda_i J^{\frac{-1}{3}}$ and $\bar{\lambda}_i$ represent the primary strains of the generic strain tensor.

Equation 4 shows how the initial shear modulus (μ_0) and bulk modulus (K_0) of the Moony–Rivlin model are obtained.

$$\mu_0 = 2\left(C_{10} + C_{01}\right). \quad K_0 = \frac{2}{D}. \tag{4}$$

Equation 5 [17] expresses the function of strain energy per unit volume in the Neo-Hooke model [30].

$$U = C_{10}\left(\bar{I}_1 - 3\right) + \frac{1}{D_1}((J^{el} - 1))^2, \tag{5}$$

where C_{10} and D_1 represent time-dependent variables, and $\bar{I}_1$ denotes the initial constant of the strain-forming portion described in terms of the shear tensile stresses as follows:

$$\bar{I}_1 = \bar{\lambda}_1^2 + \bar{\lambda}_2^2 + \bar{\lambda}_3^2 \tag{6}$$

where $(i = 1,2,3)$, $\bar{\lambda}_i = \lambda_i J^{\frac{-1}{3}}$, and $\bar{\lambda}_i$ are the tensor's primary strains of overall strain.

Equation 7 exhibits how the Neo-Hooke model's initial shear modulus (μ_0) and bulk modulus (K_0) are calculated.

$$\mu_0 = 2\left(C_{10}\right) \quad K_0 = \frac{2}{D}. \tag{7}$$

On the other hand, the shear and viscoelastic bulk moduli are computed in the Prony series and the time function as follows [30]:

$$G(\tau) = G_0\left(g_\infty + \sum_{i=1}^{N} g_i e^{-\frac{\tau}{\tau_i}}\right), \tag{8}$$

$$k(\tau) = k_0\left(k_\infty + \sum_{i=1}^{N} k_i e^{-\frac{\tau}{\tau_i}}\right) \tag{9}$$

where N denotes the number of terms in the Prony series, G_0 and K_0 represent the shear modulus and bulk modulus, respectively,τ_i represents a time constant, and k_i and g_i indicate the constants for the Prony series domain. Long shear modulus (g^∞) and without-dimension bulk modulus (k^∞) are the two terms used in these equations.

References

1. Kamanli A, Karaca-Acet G , Kaya A, Koc M, Yildirim H (2010) Conventional physical therapy with lumbar traction; clinical evaluation and magnetic resonance imaging for lumbar disc herniation. Bratislava Med J; 111(10): 541–544. http://bmj.fmed.uniba.sk/2010/11110-03.
2. Wang H (2020) Quantifying the ranges of relative motions of the intervertebral discs and facet joints in the normal cervical spine. J Biomech 112:110023. https://doi.org/10.1016/j.jbiomech.2020.110023
3. Lipson SJ, Muir H (1980) Volvo award in basic science. Proteoglycans in experimental intervertebral disc degeneration. Spine (Phila Pa 1976). 1981;6(3):194–210. https://doi.org/10.1097/00007632-198105000-00002..
4. Moussa A, Hacene A, Hammoudi M (2018) Numerical shape optimization of cervical spine disc prosthesis; 36:56–69. https://doi.org/10.4028/www.scientific.net/JBBBE.36.56.
5. Villarraga ML, Kurtz SM (2016) 14 the clinical performance of UHMWPE in the Spine, 3rd (edn). Elsevier Inc., Amsterdamhttps://doi.org/10.1016/B978-0-323-35401-1.00014-4
6. Chethan KN, Mohammad Z, Shyamasunder Bhat N, Satish Shenoy B (2020) Optimized trapezoidal-shaped hip implant for total hip arthroplasty using finite element analysis. Cogent Eng . https://doi.org/10.1080/23311916.2020.1719575.
7. Chethan KN, Shyamasunder Bhat N, Zuber M, Satish Shenoy B (2021) Finite element analysis of hip implant with varying in taper neck lengths under static loading conditions. Comput Methods Programs Biomed 208:106273. https://doi.org/10.1016/j.cmpb.2021.106273
8. Shahzad M, Kamran A, Siddiqui MZ, Farhan M (2015) Mechanical characterization and FE modelling of a hyperelastic material. Mater Res 18(5):918–924. https://doi.org/10.1590/1516-1439.320414
9. Muhr AH (2005) Modeling the stress-strain behavior of rubber. Rubber Chem Technol 78(3):391–425. https://doi.org/10.5254/1.3547890
10. Khajehsaeid H, Arghavani J, Naghdabadi R, Sohrabpour S (2014) A visco-hyperelastic constitutive model for rubber-like materials: a rate-dependent relaxation time scheme. Int J Eng Sci 79:44–58. https://doi.org/10.1016/j.ijengsci.2014.03.001
11. Carlescu V, Adrian Rusu M, Prisacaruand G, Olaru DN (2015) Experimental charactrization and fem simulation on uniaxial tensile and compression of Dielectric elastomers. No. Lxv, 2015. https://www.researchgate.net/publication/281677432
12. Pouriayevali H, Guo YB, Shim VPW (2011) A visco-hyperelastic constitutive description of elastomer behaviour at high strain rates. Procedia Eng. 10:2274–2279. https://doi.org/10.1016/j.proeng.2011.04.376
13. Nazouri M, Seifzadeh A, Masaeli E (2020) Characterization of polyvinyl alcohol hydrogels as tissue-engineered cartilage scaffolds using a coupled finite element-optimization algorithm. J Biomech 99:109525. https://doi.org/10.1016/j.jbiomech.2019.109525
14. Seifzadeh A, Oguamanam DC, Papini M (2012) Evaluation of the constitutive properties of native, tissue engineered, and degenerated articular cartilage. Clin Biomech (Bristol, Avon) 27(8):852–858. https://doi.org/10.1016/j.clinbiomech.2012.04.005
15. Mahdian M, Seifzadeh A, Mokhtarian A, Doroodgar F (2021) Characterization of the transient mechanical properties of human cornea tissue using the tensile test simulation. Mater. Today Commun; 26, p. 102122. https://doi.org/10.1016/J.MTCOMM.2021.102122.
16. Niki Y, Seifzadeh A (2021) Characterization and comparison of hyper-viscoelastic properties of normal and osteoporotic bone using stress-relaxation experiment. J Mech Behav Biomed Mater; 123, pp 104754. https://doi.org/10.1016/j.jmbbm.2021.104754.
17. Mo ZJ, Bin Zhao Y, Wang LZ, Sun Y, Zhang M, Fan YB (2014) Biomechanical effects of cervical arthroplasty with U-shaped disc implant on segmental range of motion and loading of surrounding soft tissue. Eur Spine J; 23(3):613–621. https://doi.org/10.1007/s00586-013-3070-4.
18. Bowden AE, Oneida E, Bergström J (2009) Computer modeling and simulation of UHMWPE. UHMWPE Biomater. Handb., pp 519–532. https://doi.org/10.1016/B978-0-12-374721-1.00035-3
19. Kanaga KKS et al (2008) Friction and wear behavior of ultra-high molecular weight polyethylene as a function of polymer crystallinity. Acta Biomater 4(5):1401–1410. https://doi.org/10.1016/j.actbio.2008.02.022
20. Seifzadeh A, Wang J, Oguamanam DCD, Papini M (2011) A nonlinear biphasic fiber-reinforced porohyperviscoelastic model of articular cartilage incorporating fiber reorientation and dispersion. J Biomech Eng ;133(8), pp. 1–8. https://doi.org/10.1115/1.4004832.
21. CAE User (2014) Abaqus theory manual. Abaqus 6.13 Doc., no. Dassault Systemes Simulia Corp., Providence, RI, USA.
22. Balalidehkordi R, Seifzadeh A, Farhatnia F, Mokhtarian A (2022) Prediction of articular cartilage transient response using a constitutive equation approach considering its time-varying material properties. J Brazilian Soc Mech Sci Eng 44(6):1–14. https://doi.org/10.1007/s40430-022-03488-w
23. Seifzadeh A, Oguamanam DC, Trutiak N, Hurtig M, Papini M (2012) Determination of nonlinear fibre-reinforced biphasic poroviscoelastic constitutive parameters of articular cartilage using stress relaxation indentation testing and an optimizing finite element analysis. Comput Methods Programs Biomed 107(2):315–326. https://doi.org/10.1016/j.cmpb.2011.07.004
24. Bruce V. Darden, II, MD. ProDisc-C Cervical Disk Arthroplasty. Semin Spine Surg 24:8–13 © 2012 Elsevier Inc. All rights reserved. doi.org/https://doi.org/10.1053/j.semss.2011.11.003
25. Bhattacharya S., Roy S., Rana M. et al (2019) Biomechanical performance of a modified design of dynamic cervical implant compared to conventional ball and socket design of an artificial intervertebral disc implant a finite element study shambo. J Mech Med Biol; 19:1950017. https://doi.org/10.1142/S0219519419500179.
26. Bhattacharya S, Goel VK, Liu X, Kiapour A, Serhan HA (2011) Models that incorporate spinal structures predict better wear performance of cervical artificial discs. Spine J 11(8):766–776. https://doi.org/10.1016/j.spinee.2011.06.008
27. Store HISO (2011) International Standard intervertebral spinal disc prostheses. https://www.iso.org/en/ics/11.040.40.html
28. Ogden RW (1972) Large deformation isotropic elasticity – on the correlation of theory and experiment for incompressible rubberlike solids. Proc R Soc Lond A Math Phys Sci 326(1567):565–584. https://doi.org/10.1098/rspa.1972.0026
29. Simo JC, Taylor RL (1991) Quasi-incompressible finite elasticity in principal stretches. Continuum basis and numerical algorithms. Comput Methods Appl Mech Eng 85(3):273–310. https://doi.org/10.1016/0045-7825(91)90100-K
30. Lai WM, Mow VC (1896) Third international congress of dermatology. Br J Dermatol 8(10):389–399. https://doi.org/10.1111/j.1365-2133.1896.tb16883.x

Publisher's Note Springer Nature remains neutral with regard to jurisdictional claims in published maps and institutional affiliations.